

# On the Decomposition of Synthetic Gibbsite Studied by Neutron Thermodiffraction

José Manuel Rivas Mercury,<sup>‡</sup> Pilar Pena,<sup>†</sup> and Antonio H. de Aza  
Instituto de Cerámica y Vidrio, CSIC; Kelsen, 5, 28049 Cantoblanco, Madrid, Spain

Denis Sheptyakov

Laboratory for Neutron Scattering, ETH Zürich & PSI Villigen, 5232 Villigen PSI, Switzerland

Xavier Turrillas<sup>§</sup>

Eduardo Torroja Institute for Construction Sciences, C.S.I.C., 28033 Madrid, Spain

**The thermal decomposition mechanism of synthetic  $\text{Al}(\text{OH})_3$  (gibbsite) was studied *in situ* by neutron thermodiffraction in an ambient atmosphere from room temperature to 600°C with 50°C steps. Gibbsite decomposed to yield  $\text{AlO} \cdot (\text{OH})$  (boehmite) and then poorly crystallized  $\gamma\text{-Al}_2\text{O}_3$ . Rietveld analysis was used to refine the cell parameters' variation of gibbsite and its thermal expansion coefficients were obtained: for the *a*-axis:  $15 \pm 1 \times 10^{-6} \text{ K}^{-1}$ , for *b*:  $10 \pm 2 \times 10^{-6} \text{ K}^{-1}$ , and for *c*:  $17 \pm 2 \times 10^{-6} \text{ K}^{-1}$ .**

## I. Introduction

ALUMINUM trihydroxide,  $\text{Al}(\text{OH})_3$  (gibbsite), is the main mineral phase present in tropical bauxites and clays<sup>1</sup> and it is synthesized by the industrial Bayer process.<sup>2,3</sup> Currently, it is used to a great extent as a catalyst support.<sup>4</sup> It is also the starting material to obtain metallurgical-grade alumina for the production of metallic aluminum in the Hall–Heroult process and the precursor to produce various types of transitional aluminas for ceramic applications. The most widely used among them is  $\gamma\text{-Al}_2\text{O}_3$ , because of its great adsorptive power and its catalytic properties. Consequently, there is a rich area of chemical engineering built around this process. All these synthetic routes involve its decomposition, which stimulates the interest in its dehydration and topics related to it, such as its thermal stability and reaction kinetics.

Among the techniques used to understand the dehydration, conventional thermal analysis has been widely used, e.g., thermogravimetric (TGA), differential thermal analysis (DTA), and differential scanning calorimetry (DSC).<sup>5,6</sup> For instance, Paulik *et al.*<sup>7,8</sup> explained the gibbsite decomposition in terms of its crystallinity. Rouquerol *et al.*<sup>9</sup> interpreted the gibbsite dehydration as a hydrothermal decomposition process. They suggested that inside the polycrystalline grains, a water overpressure is developed—close to hydrothermal conditions—when the temperature increases. They studied the influence of the grain size, the vapor pressure, and the heating rate on the dehydration process. These same authors in a later work<sup>6</sup> determined a

differential enthalpy value (ranging from 77 to 88 kJ/mol) for the dehydration process of gibbsite as a function of grain size and external pressure. Also, they reported that depending on the pressure applied to a gibbsite powder with a particle size distribution  $\sim 1 \mu\text{m}$ , the products found were different: for 0.04 mmHg, the dehydration was yielding a non-crystalline product, for 1 mmHg, a mixture of boehmite and  $\rho$  alumina, and for the atmospheric pressure, both boehmite and  $\chi$  alumina were observed.

Peric *et al.*<sup>10</sup> have been investigating the dehydroxylation of gibbsite into boehmite using DSC analysis under constant heating experiments in the temperature range of 453°–673°C at heating rates from 2.5 to 20°C/min. They reported an activation energy for the first stage (dehydroxylation) of  $137 \pm 10 \text{ kJ/mol}$ .

Unfortunately, although those investigations based on thermal methods provide very valuable thermodynamic knowledge, they do not allow a direct *in situ* identification of the phases formed. One *in situ* experiment using transmission electron microscopy (TEM) has been reported by Kogure<sup>11</sup> but under conditions of temperature that are not completely controlled and under vacuum; the sequence of gibbsite dehydration by electron-beam irradiation is in agreement with other experiments under vacuum conditions. In another publication of Neissendorfer *et al.*,<sup>12</sup> synchrotron X-ray experiments conducted *in situ* to dehydrate  $\text{Al}(\text{OH})_3$  at very fast heating rates (180°C/min), in the temperature range from 20° to 1000°C have been described. As far as we are aware, no other work on the gibbsite decomposition using neutron thermodiffraction had been reported in the literature.

The aim of the present work was to study *in situ* by neutron diffraction (ND) the dehydration mechanism and kinetics of a synthetic gibbsite and also to obtain data about its thermal expansion, which were not available in the literature.

## II. Experimental Procedure

### (1) Description of the Specimen

A synthetic gibbsite prepared by the Bayer process and supplied by Alcoa, San Ciprián, Lugo, Spain, was used. The chemical analyses of gibbsite, carried out by X-ray fluorescence spectroscopy (XRF, Magi X; Phillips, the Netherlands) and flame emission spectrometry for alkaline analyses (Na and K) (FES, 2100; Perkin Elmer), indicated that the gibbsite was composed of 65.01%  $\text{Al}_2\text{O}_3$ , 0.21%  $\text{Na}_2\text{O}$ , 0.1%  $\text{TiO}_2$ , 0.04%  $\text{SiO}_2$ , 0.03%  $\text{CaO}$ , 0.006%  $\text{MgO}$ , and 0.001%  $\text{K}_2\text{O}$ . The sample experienced an ignition loss of 34.61% and had a purity grade of 99.7%. Its average particle size (110  $\mu\text{m}$ ) was due to the agglomeration of smaller crystals. Original gibbsite were attrition milled with

W. Lee—contributing editor

Manuscript No. 21465. Received February 10, 2006; approved May 23, 2006.

This work was supported by MCYT Plan Nacional de Materiales CICYT Project MAT-2003-08331-CO2-01. The ND data of this work were acquired at the Swiss Spallation Neutron Source, Paul Scherrer Institute (Switzerland), with the allocation beam time for experiment number II/02 S-18.

<sup>†</sup>Author to whom correspondence should be addressed. e-mail: ppena@icv.csi.es

<sup>‡</sup>Present address: Centro Federal de Educação Tecnológica do Maranhão, CEFET-MA Av. Getúlio Vargas, 04 Monte Castelo, CEP 65025-001, São Luis, MA, Brasil.

<sup>§</sup>Present address: ESRF, 38043 Grenoble, France.

partially stabilized zirconia (PSZ)-zirconia balls in isopropanol for 24 h; the average grain size of milled gibbsite was 1.5  $\mu\text{m}$ . The specific surface area of the original sample was 0.07  $\text{m}^2/\text{g}$ . After milling, this value increased to 31.96  $\text{m}^2/\text{g}$  as determined by Brunauer–Emmett–Teller method (BET). Conventional X-ray diffraction (XRD) and ND at room temperature of both samples indicated that they were single phase crystalline gibbsites.

## (2) Thermal Analysis

DTA–TGA analysis (STA 409, Netzsch, Germany) studies were conducted at variable constant heating rates of 2, 5, 10, and 20  $^\circ\text{C}/\text{min}$  up to 1100  $^\circ\text{C}$  in air, using Pt crucibles and  $\alpha\text{-Al}_2\text{O}_3$  as a reference.

## (3) X-Ray Diffraction

The XRD patterns were acquired using a Kristalloflex D5000 (Siemens, Germany) diffractometer (Bragg–Brentano geometry) with silicon powder as an internal standard for  $d$ -spacings.

## (4) Neutron Thermodiffraction

The high-temperature powder ND experiments were performed with the HRPT instrument<sup>13</sup> of SINQ (Paul Scherrer Institute, Switzerland) with a wavelength of 1.886  $\text{\AA}$ , operating in high-intensity mode. The angle domain scanned was from 3  $^\circ$  to 163  $^\circ$  2- $\theta$ .

Powder specimens were introduced in steel tubes of 8 mm internal diameter and 80 mm length. A few grams filled the tubes up to 60 mm height. The beam size approximately 40 mm high ensured that the diffracting volume was statistically representative of the sample. The steel tubes were inserted into the furnace attached to the instrument, capable of attaining 1000  $^\circ\text{C}$ . The heating element, a cylinder made of tantalum, generated a constant temperature region of several centimeters along its axis. The temperature was controlled with two chromel–alumel thermocouples placed in direct contact with the sample container and it was stable within an accuracy of  $\pm 5^\circ\text{C}$ . The sample containers remained open to the atmosphere during the heating experiment.

Before heating, diffraction data were taken at room temperature for approximately 1 h, which ensured good histogram statistics. The same data collection strategy was followed for subsequent stages at temperatures ranging from 100  $^\circ\text{C}$  to 600  $^\circ\text{C}$  with 50  $^\circ\text{C}$  steps, with 1 h dwelling periods to ensure good statistics. The temperature increase rate between stages was 20  $^\circ\text{C}/\text{min}$ .

## (5) Data Analysis

General data processing and plotting were conducted with the help of the commercial package ORIGIN-7.0.<sup>14</sup> Rietveld analysis was performed with FULLPROF.<sup>15</sup>

The diffraction peak shapes of the various phases were fitted to Gaussian curves with the help of procedures written in IDL.<sup>16</sup>

## III. Results and Discussion

### (1) Crystal Structure of Gibbsite up to 400 $^\circ\text{C}$

(A) *Rietveld Analysis*: There are two entries in ICSD for gibbsite, and both gave drastically different values.<sup>17,18</sup> According to Saalfeld,<sup>18</sup> gibbsite has a monoclinic crystal structure ( $P2_1/n$ ,  $a = 8.684(1)$   $\text{\AA}$ ,  $b = 5.078(1)$   $\text{\AA}$ ,  $c = 9.736(2)$   $\text{\AA}$ ,  $\beta = 94.54(1)$ , and  $V = 428.0$   $\text{\AA}^3$ ), and exhibits a tabular pseudo-hexagonal habit. The structure can be regarded as stacked hexagonal close-packed (hcp) layers with open planes between successive sheets. Each Al cation is octahedrally coordinated to six OH groups and each hydroxyl group is coordinated to two Al cations, leaving vacant one octahedral site. Alternatively, it can be envisaged as double layers of hcp hydroxyl groups stacked in an AB BA sequence.<sup>17,19</sup>

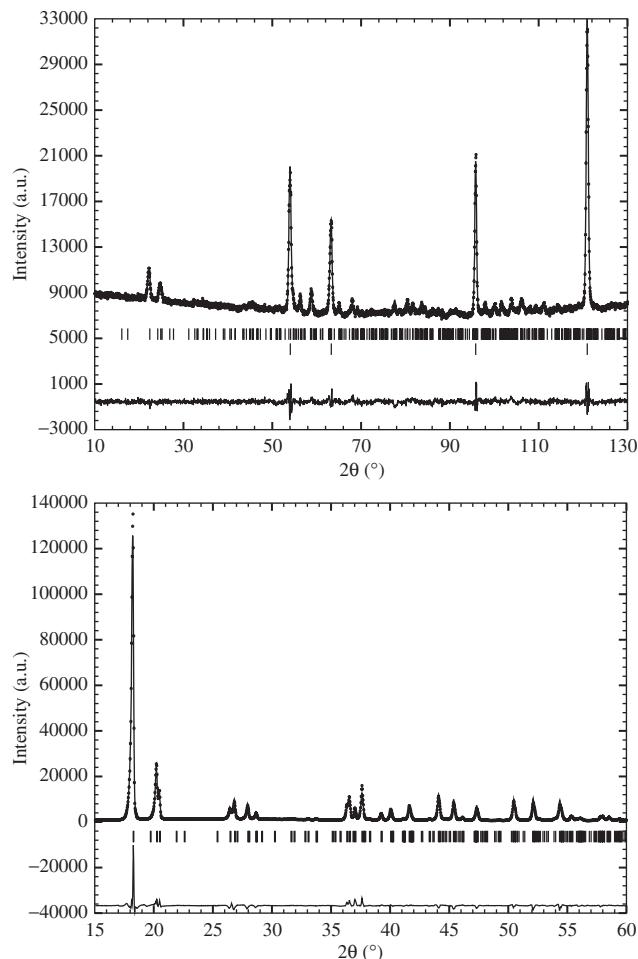


**Fig. 1.** Simultaneous Rietveld refinement of room-temperature neutron (top) and X-ray (bottom) diffraction patterns for gibbsite. The vertical lines correspond to the Bragg peaks of the different phases. Superior ones to gibbsite and inferior ones to iron.

The ND patterns from 10.05 to 140 ( $2\theta$ ) were refined using the program FULLPROF and following the guidelines of McCusker *et al.*<sup>20</sup> (Fig. 1). A pseudo-Voigt function was used. Soft (16 in total) constraints for the distances Al–O and O–H were introduced. The refined parameters were as follows: lattice parameters, zero-shift, background coefficients, Caglioti,<sup>21</sup> full-width at half-maximum (U, V, W), mixing coefficients of the pseudo-Voigt function, and asymmetry of the Bragg peaks.<sup>22,23</sup> The Debye–Waller factor was set to the overall mode. Owing to the presence of steel reflections, because of the sample holder, a similar scheme of fitting parameters was used to fit them. For the room-temperature diffraction patterns, both X-ray and neutron data were fitted simultaneously, introducing a preferential orientation parameter (March’s Dollase) for direction 001.<sup>24,25</sup> The results of ND and XRD patterns refinement for gibbsite at room temperature are given in Table I. The agreement factors attained were acceptable.

It is worth mentioning that some authors have reported<sup>26,27</sup> (based on *ab initio* calculations) new positions for hydrogen atoms. As X-ray, in principle, is less accurate than neutrons to determine hydrogen positions, we attempted to locate hydrogens from our ND data. Unfortunately, when the hydrogen position variables were set free during the Rietveld analysis, the computations became unstable, even with soft constraints for O–H distances, and it was not possible to locate the hydrogen atoms. However, upon fixing the hydrogens to the positions given by Saalfeld and Wedde<sup>18</sup> in our experimental work and liberating the rest of the atomic positions, the refinements converged and gave values as low as 8.6% (Table II). Most likely, we were not

**Table I. Positional Parameters for Monoclinic Gibbsite Obtained in the Structural Refinement**

S.G. P 21/n			
Atomic coordinates			
Atom	<i>x</i>	<i>y</i>	<i>z</i>
Al1	0.185 (0.005)	0.462 (0.006)	0.991 (0.005)
Al2	0.322 (0.005)	0.074 (0.006)	0.987 (0.004)
O1	0.178 (0.002)	0.229 (0.005)	0.901 (0.002)
O2	0.656 (0.002)	0.655 (0.004)	0.894 (0.002)
O3	0.484 (0.003)	0.124 (0.004)	0.890 (0.001)
O4	0.988 (0.003)	0.650 (0.002)	0.879 (0.002)
O5	0.298 (0.003)	0.719 (0.005)	0.897 (0.001)
O6	0.811 (0.003)	0.156 (0.005)	0.901 (0.002)
H1	0.099	0.171	0.887
H2	0.588	0.559	0.900
H3	0.479	0.093	0.805
H4	0.948	0.806	0.868
H5	0.278	0.736	0.808
H6	0.813	0.121	0.809

All atoms in Wickoff position 4(e).

able to determine the hydrogen location because the 14 atomic sites are in general positions; hence, there were too many coordinates to be refined. For the refinements at higher temperatures, the hydrogen positions were set to room-temperature values. Regarding the cell parameters, it is worth comparing the theoretical with the experimental ones. The data gathered in Table II clearly show that our experimental data are closer to the Saalfeld values.<sup>18</sup>

(B) *Cell Parameter Variation:* The variation of the unit cell volume is represented in Fig. 2. The gibbsite unit cell parameters' variation with temperature was analyzed up to 400°C. It is continuous between 20° and 250°C, but above this temperature, the unit cell parameters and volume do not vary in the expected way because of the collapse of its crystalline structure (Table III). In this table, the cell parameters up to 350°C are included. Although the cell parameters above 250°C were refined, the statistical indicators are not very good as the crystal structure is about to collapse.

The temperature dependences of these parameters between 20° and 250°C were fitted to:

$$a = (8.644 \pm 0.001) + (1.26 \pm 0.03)10^{-4}T$$

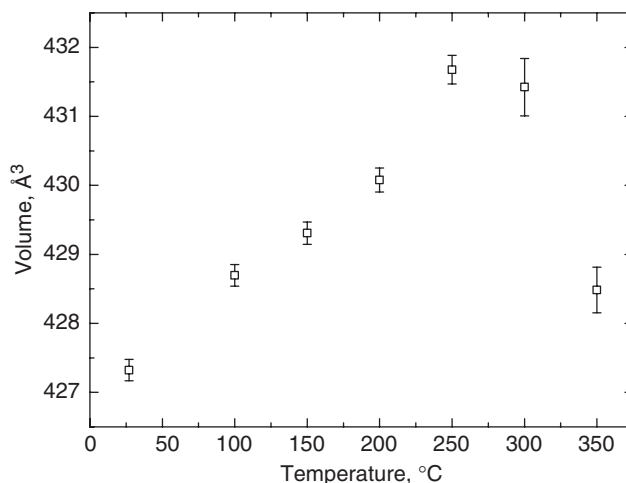
$$b = (5.062 \pm 0.001) + (5.2 \pm 0.2)10^{-5}T$$

$$c = (9.682 \pm 0.001) + (1.7 \pm 0.4)10^{-4}T, \text{ and}$$

$$V = (422.3) + (0.0175 \pm 0.0003) \cdot 10^{-3}T$$

where T is the absolute temperature.

The thermal expansion coefficients were calculated from these linear relationships; thus, the gibbsite mean thermal expansion

**Fig. 2.** Variation of gibbsite cell volume with temperature.

coefficient between 20° and 250°C obtained along the *a*-axis is  $15 \pm 1 \times 10^{-6} \text{ K}^{-1}$ ,  $10 \pm 2 \times 10^{-6} \text{ K}^{-1}$  along the *b*-axis, and  $17 \pm 2 \times 10^{-6} \text{ K}^{-1}$  along the *c*-axis.

## (2) Phase Evolution of Gibbsite with Temperature up to 700°C

(A) *Conventional Thermal Analysis:* In order to determine the effect of heating rate on the dehydration reaction pathways of gibbsite, DTA curves of the fine-grained crystalline gibbsite were obtained at different heating rates. These previous experiments permitted to set the optimal conditions to identify separate steps of the dehydration process, at a heating rate of 10°C/min.

Figure 3 shows TGA (DTA–TGA) curves, recorded at 10°C/min, corresponding to both types of crystalline gibbsite (grain size average of 110 and 1.5 μm, respectively). As a whole, it has been observed that both fine and coarse-particle specimens follow similar paths, showing dehydration curves analogous to those described in the literature<sup>28</sup> (Fig. 3). The coarse and fine-grained gibbsite show a small endothermic peak at ≈215°C, a sharp endothermic peak at ≈305°C, and a weaker endothermic peak at ≈500°C. But it is to be noticed that intensities are significantly reduced for finer particle size samples. The total weight loss observed on the TGA curves in the temperature range 200°–700°C was 34.61 wt% (Fig. 3). This total loss of 34.61 wt% (Fig. 3(a)) agrees very well with the theoretical value of 34.72 wt% for the dehydration reaction.

The DTA–TGA curve can be interpreted as follows: the gibbsite decomposition takes place in several steps. At a temperature slightly above 200°C, boehmite appears. In the range of 200°–280°C, only a small weight loss is observed (7% approx.). This is due to the fact that not all the water is released. Most of it becomes trapped inside the coarse gibbsite grains under a relatively high overpressure. As the temperature increases—

**Table II. Refined Structural Parameters of Gibbsite (Al(OH)<sub>3</sub>) Between 20° and 350°C Using the Monoclinic Crystal Structure (P2<sub>1</sub>/n Space Group)**

T(°C)	<i>a</i> ± 2σ	<i>b</i> ± 2σ	<i>c</i> ± 2σ	β ± 2σ	<i>V</i> ± 2σ	B <sub>iso</sub> ± 2σ	R <sub>wp</sub>	χ <sup>2</sup>	R <sub>b</sub>
20	8.6797 ± 0.0005	5.0756 ± 0.0003	9.7329 ± 0.0005	94.580 ± 0.005	427.41 ± 0.04	0.7 ± 0.1	13.20	3.50	8.60
100	8.6897 ± 0.0004	5.0799 ± 0.0003	9.7471 ± 0.0005	94.656 ± 0.005	428.84 ± 0.04	0.8 ± 0.1	13.10	3.30	8.13
150	8.6960 ± 0.0005	5.0823 ± 0.0003	9.7549 ± 0.0005	94.714 ± 0.005	429.67 ± 0.04	0.8 ± 0.2	14.20	3.66	7.79
200	8.7023 ± 0.0005	5.0850 ± 0.0003	9.7643 ± 0.0005	94.775 ± 0.005	430.58 ± 0.05	0.8 ± 0.2	13.50	3.17	6.31
250	8.7091 ± 0.0007	5.0864 ± 0.0005	9.7703 ± 0.0007	94.900 ± 0.006	431.22 ± 0.06	1.1 ± 0.3	13.60	3.23	7.72
300	8.713 ± 0.001	5.0845 ± 0.0006	9.7742 ± 0.0010	94.994 ± 0.009	431.37 ± 0.08	2.3 ± 0.3	13.80	3.48	15.7
350	8.696 ± 0.001	5.085 ± 0.002	9.783 ± 0.004	94.89 ± 0.03	431.0 ± 0.3	3.1 ± 0.3	15.66	5.37	15.8

To estimate the “goodness of fit” three reliability factors (R<sub>wp</sub>, χ<sup>2</sup>, and R<sub>b</sub>) were calculated and in all cases. 2σ represent the error bars assigned to every experimental value.

**Table III. Phases Identified by ND Along the *in situ* Experiment and by XRD on Samples Heated at Different Temperatures for 1 h and Quenched**

Temperature (°C)	Crystalline phases by XRD, on heated and quenched samples		Crystalline phases by ND <i>in situ</i> experiment
	Coarse grains	Fine grains	
27	Al(OH) <sub>3</sub>	Al(OH) <sub>3</sub>	Al(OH) <sub>3</sub>
100	—	—	Al(OH) <sub>3</sub>
150	—	—	Al(OH) <sub>3</sub>
200	—	—	Al(OH) <sub>3</sub> +AlO·(OH)
250	Al(OH) <sub>3</sub> +AlO·(OH)	Al(OH) <sub>3</sub> +AlO·(OH)	Al(OH) <sub>3</sub> +AlO·(OH)
300	—	—	Al(OH) <sub>3</sub> +AlO·(OH)
350	—	—	Al(OH) <sub>3</sub> +AlO·(OH)
400	—	—	Al(OH) <sub>3</sub> +AlO·(OH)
450	AlO·(OH)+ $\chi$ -Al <sub>2</sub> O <sub>3</sub>	AlO·(OH)+ $\chi$ -Al <sub>2</sub> O <sub>3</sub>	AlO·(OH)+ $\chi$ -Al <sub>2</sub> O <sub>3</sub>
500	—	—	AlO·(OH)+ $\chi$ -Al <sub>2</sub> O <sub>3</sub>
550	—	—	AlO·(OH)+ $\chi$ -Al <sub>2</sub> O <sub>3</sub>
600	—	—	$\chi$ -Al <sub>2</sub> O <sub>3</sub>
700	$\chi$ -Al <sub>2</sub> O <sub>3</sub>	$\chi$ -Al <sub>2</sub> O <sub>3</sub>	

The reflections (002) for Al(OH)<sub>3</sub> (gibbsite), (020) for AlO·(OH) (boehmite), and (440) for (chi alumina)  $\chi$ -Al<sub>2</sub>O<sub>3</sub> were used. XRD, X-ray diffraction; ND, neutron diffraction.

above 280°C—the coarse gibbsite grains shatter, suddenly freeing water vapor. This is manifested by the fast weight loss on the TGA curve of coarse-grained gibbsite ( $\approx$ 19% between 280° and 320°C) (Fig. 3(a)). This overpressure inside the gibbsite grains could favor the boehmite formation. In the fine-grained gibbsite, this effect is very weak. The XRD patterns of both fine and coarse gibbsite after heating at 250°C show a new peak at 14.4°(2 $\theta$ ) corresponding to boehmite (AlO·(OH)) along with gibbsite peaks. It may be concluded that in fine crystalline gibbsite ( $\approx$ 1.5  $\mu$ m), the formation of boehmite occurs when calcining between 250° and 400°C.

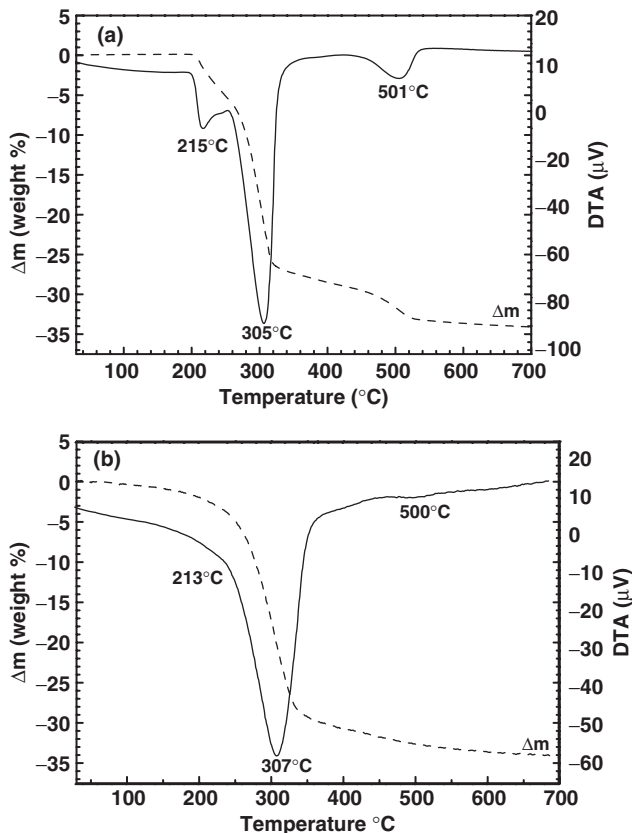


**Fig. 3.** (a) Differential thermal analysis–thermogravimetric (DTA–TGA) curves for coarse-grained gibbsite at 10°C/min; (b) DTA–TGA results for fine-grained gibbsite at 10°C/min.

The endothermic peak with maxima at  $\approx$ 500°C of both samples is due to  $\chi$ -Al<sub>2</sub>O<sub>3</sub> formation. XRD of both samples heated 1 h at 400°C shows  $\chi$ -Al<sub>2</sub>O<sub>3</sub> and boehmite (Table III).

(B) *Neutron Thermodiffraction:* In order to identify the crystalline phases formed *in situ* at each temperature, the dehydration of gibbsite has been monitored by using ND.

A general picture of the diffraction patterns as the temperature increases is shown in Fig. 4. The specimen of synthetic gibbsite studied had 34.61 wt% of water. Neutrons interact with hydrogen atoms, producing a significant incoherent scattering (larger than any other atomic species present in the sample) in all directions manifested by a notorious increase of background in the diffraction patterns. This fact explains the progressive diminution of background with temperature that can be observed in the ND patterns in Fig. 4.

The phase transformations were directly observed upon temperature increases from 200° to 600°C. The diffraction peaks of Al(OH)<sub>3</sub> were present up to 400°C. The intermediate-phase boehmite (AlO·(OH))<sup>29</sup> existed between 200° and 550°C, and the transition product— $\chi$ -Al<sub>2</sub>O<sub>3</sub><sup>30</sup> alumina was observed above 500°C (Fig. 4).

At the end of the experiment (600°C), the background was still very high, which may indicate a significant amount of poor or non-crystalline phases. Diaspore, the other polymorph phase

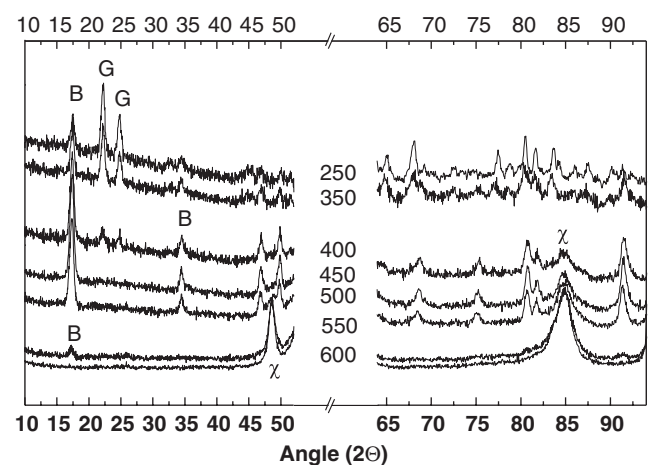


**Fig. 4.** Neutron diffraction patterns of gibbsite at various temperatures (°C). B stands for boehmite, G for gibbsite, and  $\chi$  for  $\chi$ -Al<sub>2</sub>O<sub>3</sub>. The diffraction patterns include the actual background counts (it is not an offset to separate the patterns).

of  $\text{AlO} \cdot (\text{OH})$ ,  $\gamma$ , and  $\alpha\text{-Al}_2\text{O}_3$  were not detected during the dehydration process at the temperature interval of  $20^\circ\text{--}600^\circ\text{C}$ . The crystalline phases identified in the samples treated at different temperatures are summarized in Table III. The data obtained by ND were coincident with those obtained by conventional XRD on samples heated for 1 h and quenched at different temperatures (Table III).

Assuming that the same volume of gibbsite is irradiated along the experiment and a linear relationship between the content of hydrogen and the total intensity in the diffraction patterns, the variation of the total scattering counts for every diffraction pattern provides direct information about the amount of hydrogen present in the sample at every temperature (Fig. 5(a)). In the  $250^\circ\text{--}450^\circ\text{C}$  interval, a smooth and continuous decline of the total scattering can be observed. It is attributed to the departure of OH groups as water evaporates, hence diminishing the scattering of hydrogen in the diffraction pattern. The progressive diminution of background—which can be measured with precision—provides a clear parameter that is directly related to the OH content of the sample. In Fig. 5(a), the variation of the background arbitrarily normalized to unity as a function of temperature has been represented. The curve exhibits two effects—more clearly highlighted by its derivative—which indicates that most likely water departs in two steps (Figs. 3 and 5(a)). Obviously, if we use the total scattering counts to follow the dehydration, we will have the same limitations as in the TGA approach Fig. 5(a).

The quantitative evolution of crystal phases, which disappeared and emerged as the temperature increased, was monitored through the evolution of some of their diffraction peaks, chosen for being isolated and strong enough to give values of statistical significance. More precisely, for  $\text{Al}(\text{OH})_3$  reflection (002) was used, for boehmite  $\text{AlO} \cdot (\text{OH})$ , (020), and for  $\chi\text{-Al}_2\text{O}_3$ ,

(440). Individual intensities for every phase were fitted to Gaussian curves and their areas were normalized to 1 (Fig. 5(b)). It has been assumed that the parameter used to determine the reaction progress is directly proportional to the extent of reaction and those parallel or consecutive contributions to product formation are absent.

These neutron thermodiffraction data clearly show that gibbsite decomposition does not initiate before  $250^\circ\text{C}$ , where an induction period starts, and finishes at  $500^\circ\text{C}$ .

Once  $\text{Al}(\text{OH})_3$  disappears, boehmite starts to decompose. Gibbsite and boehmite coexist for a while (from  $250^\circ$  to  $500^\circ\text{C}$  approximately),  $\sim 365^\circ\text{C}$  being the temperature at which the concentration of both phases is approximately the same (see Fig. 5(b)). This seems to indicate that boehmite formation is controlled by gibbsite decomposition.

Above  $450^\circ\text{C}$ , boehmite begins to decay to yield a hcp<sup>31</sup>  $\chi\text{-Al}_2\text{O}_3$  transition alumina, with a formation rate maximum at around  $525^\circ\text{C}$ .

All facts considered, the information obtained about the thermal behavior of gibbsite by ND is richer in detail than the Synchrotron XRD data by Neissendorfer *et al.*<sup>12</sup>

These authors observed, also, first boehmite formation and then unknown oxides with a very poor crystalline structure. But from their results, no information about the crystal evolution of gibbsite with temperature was deduced.

The experimental evidence from XRD, DTA, TGA, and ND indicates that both fine- and coarse-grained gibbsite dehydrates yielded boehmite. More precisely, for gibbsite powders with particle sizes distributions around 110 and  $1.5\ \mu\text{m}$ , an endothermic peak at approximately  $213^\circ\text{C}$  is shown. On the one hand, this observations does not agree with the work of Rouquerol *et al.*<sup>12</sup> as these authors state that the formation of boehmite phase in coarser particles might be due to the development of hydrothermal conditions inside the gibbsite. On the other hand, it is in agreement with a recent paper by Bhattacharya *et al.*<sup>28</sup> where it is stated that crystalline gibbsite, irrespective of the particle size distribution (110 and 1.5 micrometers), as long as it has a crystalline long-range order, when heated, yields boehmite. In contrast, when the long-range order is broken, i.e., the material is really amorphous, the calcination follows a path where no boehmite appears.

As the temperature increases, the pathway of decomposition for both fine- and coarse-grained specimens is the same. A weaker endothermic peak at  $\sim 500^\circ\text{C}$  on the DTA is interpreted—with the help of X-ray and ND—as boehmite dehydroxylation. This temperature marks the onset growth of  $\chi$ -alumina that remains up to  $700^\circ\text{C}$ . It is also quite clear that most of the energy furnished up to around  $400^\circ\text{C}$  is used up by the specimen to lose water in the dehydroxylation/dehydration process, as a progressive decay of the ND background is observed. Beyond this temperature, the heat is used to rearrange the crystal framework. This is also in agreement with the observations of Bhattacharya *et al.*<sup>28</sup>

#### IV. Conclusions

A novel insight into the gibbsite thermal decomposition using neutron thermodiffraction has been presented. The results show that it takes place in successive stages: dehydration of gibbsite with nucleation of boehmite and finally, dehydration of boehmite and nucleation of  $\chi$ -alumina. A partial overlapping is observed between adjacent stages and even, in a narrow temperature domain, the gibbsite dehydration occurs while  $\chi$ -alumina initiates its nucleation.

Rietveld analysis of ND patterns at different temperatures enabled to measure the cell parameters variation for gibbsite and hence to derive its thermal expansion coefficients. A monotonous linear increase is observed up to  $250^\circ\text{C}$ . At higher temperatures, while gibbsite dehydrated, it was possible to measure the cell parameters, which did not expand anymore, presumably because of the partial collapse of its crystal structure before its final disintegration.

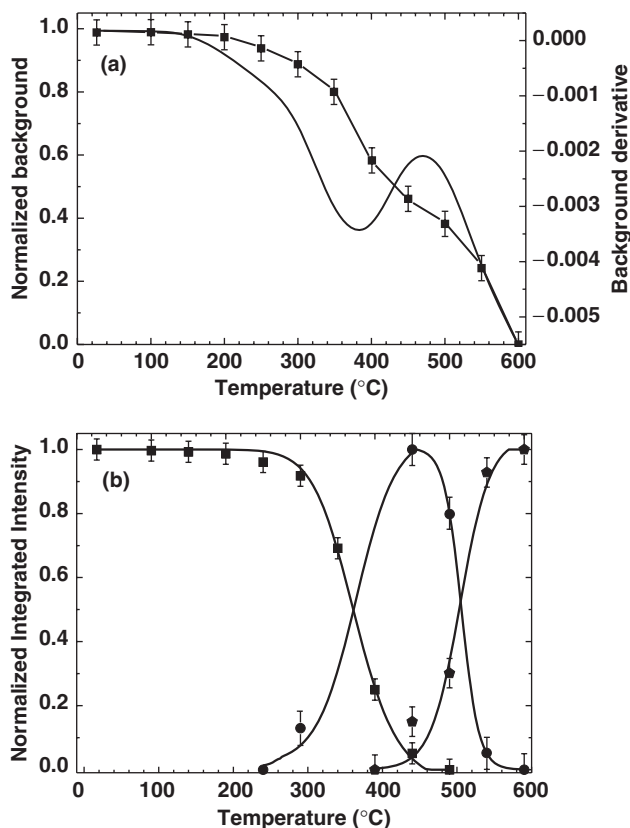


Fig. 5. (a) Variation of the total scattering counts of diffraction patterns (line with squares and error bars). The derivative curve (continuous line) highlights the temperatures at which the two mechanisms of dehydration rate are higher. (b) Integrated and normalized intensities as a function of temperature for reflections (002) of gibbsite (squares), (020) of boehmite (circles), and (440) of  $\chi\text{-Al}_2\text{O}_3$  (pentagons).

## References

- <sup>1</sup>W. A. Deer, R. A. Howie, and J. Zussman, *An Introduction to Rock Forming Minerals*. Longman Scientific and Technical, England, 1992.
- <sup>2</sup>L. D. Hart, *Alumina Chemicals Science and Technology Handbook*. The American Ceramic Society, OH, USA, 1990.
- <sup>3</sup>W. H. Gitzen, *Alumina as a Ceramic Material*. The American Ceramic Society, OH, USA, 1970.
- <sup>4</sup>P. Euzen, P. Raybaud, X. Krokidis, H. Toulhoat, J. L. LeLoarer, J. P. Jolivet, and C. Froidefont, In *Handbook of Porous Materials*, Vol. 5, Edited by F. Schüth, K. Sing, and J. Weitkamp. Wiley-VCH, New York, 2002.
- <sup>5</sup>F. Paulik, *Special Trends in Thermal Analysis*. John Wiley & Sons, Chichester, 1995.
- <sup>6</sup>J. Rouquerol, F. Rouquerol, and M. Ganteaume, "Thermal Decomposition of Gibbsite Under Low Pressures II. Formation of Microporous Alumina," *J. Catal.*, **57**, 222–30 (1979).
- <sup>7</sup>F. Paulik, J. Paulik, N. Naumann, K. Köhnke, and D. Petzold, "Mechanism and kinetics of the Dehydration of Hydrargillites. Part I," *Thermochim. Acta*, **64**, 1–14 (1983).
- <sup>8</sup>N. Naumann, K. Köhnke, J. Paulik, and F. Paulik, "Kinetics and Mechanism of the Dehydration of Hydrargillites. Part II," *Thermochim. Acta*, **64**, 15–26 (1983).
- <sup>9</sup>J. Rouquerol, F. Rouquerol, and M. Ganteaume, "Thermal Decomposition of Gibbsite Under Low Pressures I. Formation of the Boehmitic Phase," *J. Catal.*, **36**, 99–110 (1975).
- <sup>10</sup>J. Peric, R. Krstulovic, and M. Vucak, "Investigation on Dehydroxylation of Gibbsite into Boehmite by DSC Analysis," *J. Thermal Anal.*, **46**, 1339–47 (1996).
- <sup>11</sup>T. Kogure, "Dehydration Sequence of Gibbsite by Electron-Beam Irradiation in a TEM," *J. Am. Ceram. Soc.*, **82** [3] 716–20 (1999).
- <sup>12</sup>F. Neissendorfer, U. Steinike, B. P. Tolochko, and M. A. Sheromov, "On the Decomposition of Hydrargillite Investigated by Synchrotron X-Ray-Diffraction," *Nucl. Instrum. Methods Phys. Res. A-Accelerators Spectrometers Detectors Assoc. Equipment*, **261**, 219–20 (1987).
- <sup>13</sup>P. Fischer, G. Frey, M. Koch, M. Könncke, V. Pomjakushin, J. Schefer, R. Thut, N. Schlumpf, R. Bürge, U. Greuter, S. Bondt, and E. Berruyer, "High-resolution Powder Diffractometer HRPT for Thermal Neutrons at SINQ," *Physica B*, **146**, 276–8 (2000).
- <sup>14</sup>Origin version 6.5 (2002) OriginLab Corporation. One Roundhouse Plaza, Northampton, MA 01060, USA.
- <sup>15</sup>J. Rodriguez-Carvajal and J. Rodriguez-Carvajal, "FULLPROF: A Program for Rietveld Refinement and Pattern Matching Analysis"; Abstracts of the Satellite Meeting on Powder Diffraction of the XV Congress of the IUCr, p. 127, Toulouse, France, 1990.
- <sup>16</sup>Research Systems Inc. (Kodak Company), Sterling, VA 20164, USA, Program IDL, Version 5.2, 1998, www.rsinc.com.
- <sup>17</sup>H. D. Megaw, "The Crystal Structure of Hydrargillite Al(OH)<sub>3</sub>," *Z. Kristallogr.*, **87A**, 185–204 (1934).
- <sup>18</sup>H. Saalfeld and M. Wedde, "Refinement of Crystal-Structure of Gibbsite, Al(OH)<sub>3</sub>," **139**, 129–35 (1974).
- <sup>19</sup>A. Vegas and A. Ramos-Gallardo, "The Cation Array in Aluminum Oxides, Hydroxides and Oxihydroxides," *Z. Kristallogr.*, **211**, 299–312 (1996).
- <sup>20</sup>L. B. McCusker, R. B. Von Dreele, D. E. Cox, D. Louer, and P. Scardi, "Rietveld Refinement Guidelines," *J. Appl. Crystallogr.*, **32**, 36–50 (1999).
- <sup>21</sup>G. Caglioti, A. Paoletti, and F. P. Ricci, "Choice of Collimators for a Crystal Spectrometer for Neutron Diffraction," *Nucl. Instrum. Methods*, **3**, 223–8 (1958).
- <sup>22</sup>B. Van Laar and W. B. Yelon, "The Peak in Neutron Powder Diffraction," *J. Appl. Crystallogr.*, **17**, 47–54 (1984).
- <sup>23</sup>L. W. Finger, D. E. Cox, and A. P. Jephcoat, "A correction for Powder Diffraction Peak Asymmetry due to Axial Divergence," *J. Appl. Crystallogr.*, **27**, 892–900 (1994).
- <sup>24</sup>A. March, "Mathematische Theorie der Regelung Nach der Korngestalt Bei Affiner Deformation," *Z. Kristallogr.*, **81**, 285–97 (1932).
- <sup>25</sup>W. A. Dollase, "Correction of Intensities for Preferred Orientation in Powder Diffractometry. Application of the March Model," *J. Appl. Crystallogr.*, **19**, 267–72 (1986).
- <sup>26</sup>J. D. Gale, A. L. Rohl, and V. Milman, "An ab Initio Study of the Structure and Properties of Aluminum Hydroxide: Gibbsite and bayerite," *J. Phys. Chem. B*, **105**, 10236–42 (2001).
- <sup>27</sup>M. M. Digne, P. Sautet, P. Raybaud, H. Toulhoat, and E. Artacho, "Structure and Stability of Aluminum Hydroxides: A Theoretical Study," *J. Phys. Chem. B*, **106**, 5155–62 (2002).
- <sup>28</sup>I. N. Bhattacharya, S. C. Das, P. S. Mukherjee, S. Paul, and P. K. Mitra, "Thermal Decomposition of Precipitated Fine Aluminium Trihydroxide," *Scand. J. Metall.*, **33**, 211–9 (2004).
- <sup>29</sup>Powder Diffraction File Number 21-1307. ICDD. International Center for Diffraction Data, Newton Square USA (2000).
- <sup>30</sup>Powder Diffraction File Number 34-0493. ICDD. International Center for Diffraction Data, Newton Square USA (2000).
- <sup>31</sup>R. C. T. Slade, J. C. Southern, and I. M. Thompson, "Al-27 Nuclear-Magnetic-Resonance Spectroscopy Investigation of Thermal Transformation Sequences Of Alumina Hydrates. 1. Gibbsite, Gamma-Al(OH)<sub>3</sub>," *J. Mater. Chem.*, **1**, 563–8 (1991). □